SLAC-PUB-12703
August 2007

Suzaku wide-band X-ray Spectroscopy of the Seyfert 2 AGN in NGC 4945

Takeshi Itoh[1], Chris Done[2], Kazuo Makishima[1,3], Grzegorz Madejski[4], Hisamitsu Awaki[5], Poshak Gandhi[3], Naoki Isobe[3], Gulab C. Dewangan[6], Richard E. Griffthis[6], Naohisa Anabuki[7], Takashi Okajima[8,9], James Reeves[8,9], Tadayuki Takahashi[10], Yoshihiro Ueda[11], Satohi Eguchi[11], and Tahir Yaqoob[9,12]

[1] *Department of Physics, Faculty of Science, University of Tokyo, 7-3-1 Hongo, Bunkyo-ku, Tokyo, 113-0033, Japan*
titoh@amalthea.phys.s.u-tokyo.ac.jp

[2] *Department of Physics, University of Durham, South Rd, DH1 3LE Durham, UK*

[3] *Cosmic Radiation Laboratory, Institute of Physical and Chemical Research (RIKEN) 2-1 Hirosawa, Wako, Saitama, 351-0198, Japan*

[4] *Stanford Linear Accelerator Center, 2575 Sand Hill Road, Menlo Park, CA 94025, USA*

[5] *Department of Physics and Astronomy, Ehime University, Matsuyama 790-8577, Japan*

[6] *Department of Physics, Carnegie Mellon University, 5000 Forbes Avenue, Pittsburgh, PA 15213*

[7] *Department of Earth and Space Science, Osaka University, 1-1 Machikaneyama, Toyonaka, Osaka 560-0043*

[8] *Exploration of the Universe Division, Code 662, NASA Goddard Space Flight Center, Greenbelt Road, Greenbelt, MD 20771, USA*

[9] *Department of Physics and Astronomy, Johns Hopkins University, 3400 N Charles Street, Baltimore, MD 21218, USA*

[10] *Institute of Space and Astronautical Science, JAXA, 3-1-1, Yoshinodai, Sagamihara, Kanagawa, 229-8510, Japan*

[11] *Department of Astronomy, Kyoto University, Sakyo-ku, Kyoto 606-8502, Japan*

[12] *Astrophysics Science Division, Code 662, NASA Goddard Space Flight Center, Greenbelt, MD 20771, USA*

(Received 2007 0; accepted 2007 0)

Abstract

Suzaku observed a nearby Seyfert 2 galaxy NGC4945, which hosts one of the brightest active galactic nuclei above 20 keV. Combining data from the X-ray CCD camera (XIS) and the Hard X-ray Detector (HXD), the AGN intrinsic nuclear emission and its reprocessed signals were observed simultaneously. The intrinsic emission is highly obscured with an absorbing column of $\sim 5 \times 10^{24}$ cm^{-2}, and was detectable only above ~ 10 keV. The spectrum below 10 keV is dominated by reflection continuum and emission lines from neutral/ionized material. Along with a neutral iron Kα line, a neutral iron Kβ and a neutral nickel Kα line were detected for the first time from this source. The neutral lines and the cold reflection continuum are consistent with both originating in the same location. The Compton down-scattered shoulder in the neutral Fe-Kα line is $\sim 10\%$ in flux of the narrow core, which confirms that the line originates from reflection rather than transmission. The weakness of the Compton shoulder also indicates that the reflector is probably seen nearly edge-on. Flux of the intrinsic emission varied by a factor of ~ 2 within ~ 20 ks, which requires the obscuring material to be geometrically thin. Broadband spectral modeling showed that the solid angle of the neutral reflector is less than a few $\times 10^{-2} \times 2\pi$. All this evidence regarding the reprocessed signals suggests that a disk-like absorber/reflector is viewed from a near edge-on angle.

Key words: galaxies: individual (NGC 4945); galaxies: active; galaxies: Seyfert; X-rays: galaxies

1. Introduction

Our picture of nuclei of Seyfert galaxies relies on the unified scheme (Antonucci & Miller 1985), which assumes that the central source— a black hole, an accretion disk, and broad line region—is embedded within an optically thick molecular torus located at a distances larger than ~ 1 pc. Over a certain luminosity range, the structure of these main ingredients are considered almost identical in all active galactic nuclei (AGNs), and the apparent differences among individual objects are ascribed to their orientation with respect to our line of sight; the object is classified as a Seyfert 1 if the line of sight lies within the opening angle of the torus, and as a Seyfert 2 if observed through the obscuring material.

Because the nuclear intrinsic light in the optical, ultra-

Work supported in part by US Department of Energy contract DE-AC02-76SF00515

violet, and soft X-ray frequencies is absorbed by the torus, Seyfert 2 AGNs can be seen at these energies only through reprocessed emission. A large population of such obscured AGNs could make the Cosmic X-ray background (CXB; Awaki & Koyama 1993, Madau et al. 1994, Comastri et al. 1995, Gandhi & Fabian 2003, Gilli et al. 2007) provided that a typical torus is optically thick to electron scattering and subtends a large solid angle as seen from the central source. From observations of such obscured AGNs, we can investigate the circum-nuclear environment (e.g. their geometry, ionization state, etc.), thorough the reprocessed emission which would be diluted by the intrinsic emission in Seyfert 1's. From a fair number of Seyfert 2 AGNs, the ASCA satellite actually observed evidence for such emission, e.g. strong iron line complex and hard continua, in energies from a few keV to 10 keV (e.g. Iwasawa et al. 1994, Ueno et al. 1994b).

Since only hard X-rays can penetrate the obscuring material, observations in such energy range are crucial to the investigation of hidden nuclei, or even to their discovering. Many of pioneering works on this field were done with Ginga satellite, with its hard X-ray sensitivity up to ~ 30 keV (e.g. Koyama et al. 1989, Awaki et al. 1990, Awaki & Koyama 1993,Ueno et al. 1994a). The direct AGN emission, thus observed in hard X-rays, were highly absorbed even by $N_{\rm H}$ of $\gtrsim 10^{24}$ cm^{-2} (Iwasawa et al. 1993), where $N_{\rm H}$ is equivalent hydrogen column density along the line of site.

Subsequently, BeppoSAX and RXTE observed the hard X-ray emission from a number of Seyfert 2 nuclei in the $\sim$ 10–100 keV range (e.g. Ikebe et al. 2000, Matt et al. 1997, Malizia et al. 2003 and references therein). In a fraction of them, the obscuring material was found to be even opaque to Compton scattering, with $N_{\rm H} \times \sigma_{\rm T}$ reaching a few (Matt et al. 2000), where $\sigma_{\rm T}$ is the Thomson cross section. In such "Compton-thick" AGNs, accurate measurements of the intrinsic emission are quite difficult, since it appears only above ~ 10 keV with a strongly absorbed spectrum. In the most extreme cases, the direct AGN emission is completely hidden even up to ~ 100 keV.

NGC 4945 is a nearby (~ 3.7 Mpc; Mauersberger et al. 1996), edge-on (with an inclination $i \sim 78°$; Ott et al. 2001) spiral galaxy. The mass of the central black hole is constrained by H_2O megamaser observations to be $M_{\rm BH} \sim 1.4 \times 10^6 M_\odot$ (Greenhill et al. 1997). The presence of the AGN was first confirmed by the Ginga observation (Iwasawa et al. 1993), which revealed a rapidly varying nuclear flux penetrating through a heavy absorbing column of $N_{\rm H} \sim 4 \times 10^{24}$ cm^{-2}. Subsequent hard X-ray observations by the OSSE on-board CGRO (Done et al. 1996), RXTE (Madejski et al. 2000), and BeppoSAX (Guainazzi et al. 2000) showed that NGC 4945 is indeed the brightest Seyfert 2 AGN at $\gtrsim 20$ keV. The nuclear star-burst/superwind activity was also confirmed by infrared and optical observations (Chen & Huang 1997, Moorwood et al. 1996). Observation by ASCA revealed a hard continuum below ~ 10 keV, and strong iron line complex, showing that the reprocessed emission dominates in that energy range (Turner et al. 1997). Using XMM-Newton, Schurch et al. (2002) found both neutral and ionized iron lines in the reprocessed nuclear emission, but their origins (especially of the latter one) remain rather unclear even with the superb spatial resolution of Chandra (Done et al. 2003).

In the present paper, we report on a 100 ks observation of NGC 4945, performed in January 2006 with Suzaku (Mitsuda et al. 2007). Thanks to the wide band-pass of Suzaku and the good energy resolution at iron K line energy bands, we have observed simultaneously the intrinsic and the reprocessed emission of NGC 4945, both with a higher accuracy than in the previous observations. This helps us to build a consistent picture for the circum-nuclear re-processing material.

2. The Suzaku Observation of NGC 4945

Using Suzaku, we observed NGC 4945 over 2006 January 15–17, for a total duration of 230 ks. Both of the instruments on-board, i.e. the X-ray Imaging Spectrometer (XIS; Koyama et al. 2007) and the Hard X-ray Detector (HXD; Takahashi et al. 2007), were in operation in their normal modes. Event files from both instruments were screened using version 1.2 of the Suzaku pipeline processing. We used "cleaned events" files in which data of the following criteria were removed: data taken with low data rate, or with an Earth elevation angle less than 5°, or with Earth day-time elevation angles less than 20°, or during passages through or close to the South Atlantic Anomaly (SAA). Cut-off rigidity (COR) criteria of > 6 GV for the XIS and > 8 GV for the HXD were also applied.

2.1. XIS Data Analysis

In analyzing the XIS data, we used only events with grades 0, 2, 3, 4 and 6. Hot and flickering pixels were removed using `cleansis` software. From each XIS sensor, we omitted those periods which suffered from telemetry saturation. Figure 1 shows the XIS image of NGC 4945, in energy ranges of 0.3–4.5 keV (top) and 4.5–9.0 keV (bottom). While several sources can be seen in the lower energy band, the AGN emission is quite dominant in the higher energy band. In the same region, Schurch et al. (2002) detected non-nuclear point sources which are indicated with white arrows in figure 1 (top). We analyzed the XMM-Newton data of these sources, to find that their contamination to the Suzaku AGN spectra are negligible in energies higher than ~ 4.5 keV.

The bright source in the SW region in figure 1 has not been observed by any previous observations. According to its luminosity, this transient source could be a ultra luminous X-ray source (ULX) associated with NGC 4945. Readers are referred to Isobe et al. (2007) for detailed analysis of this source.

AGN spectra were extracted from the four XIS sensors within a circular region of $1'.45$ radius (corresponding to 1.56 kpc in physical size at a distance of 3.7 Mpc), indicated by a black circle in figure 1 (bottom). The background spectra were extracted from source free regions of the same CCDs. We made the response matri-

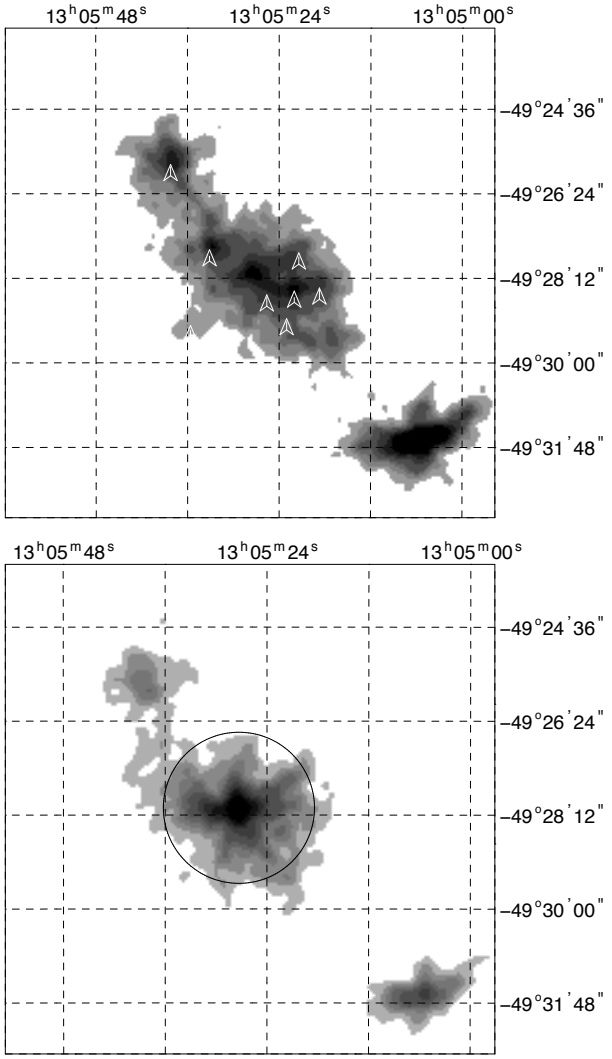

Fig. 1. Background-inclusive Suzaku XIS images of NGC 4945, in the 0.3–4.5 keV (top) and 4.5-9.0 keV band (bottom). Only events from XIS0 sensor are used. White arrows in the top panel indicate individual point sources detected by XMM-Newton (Schurch et al. 2002). Black circle in the bottom panel indicates the source extraction region. Its radius of 1′.45 corresponds to 2.00 mm on the sensor, or 1.56 kpc in physical size at the distance of 3.7 Mpc.

ces and ancillary response matrices using `xisrmfgen` and `xissimarfgen` (Ishisaki 2007) , respectively. In the following spectral analysis, we add the spectra and responses of the front-illuminated (FI) chips (XIS 0, 2, 3), and use data over an energy range of 4.5–9.0 keV to avoid possible contamination by other sources. We use an energy range of 4.5–8.0 keV for the back-illuminated (BI) XIS1 chip, due to its high background above this energy. A total net exposure of 98.8 ks was obtained from each XIS sensor, with source count rates of $(8.83 \pm 0.1) \times 10^{-2}$ cts s^{-1} for the FI chips and $(1.88 \pm 0.05) \times 10^{-2}$ cts s^{-1} for the BI chip. The source spectra were re-binned so that each bin includes at least 30 counts to enable usage of the χ^2 fit statistics.

2.2. HXD Data Analysis

The HXD-PIN spectrum was extracted from the "cleaned events" file described above. In order to estimate non X-ray background (NXB) events, we used a time-dependent instrumental background event file provided by the instrumental team. We extracted the source and the background spectra after applying an identical set of good time intervals (GTIs) to both event files. The source spectrum was further corrected for detector dead time using "pseudo events" (Kokubun et al. 2007). The dead time was $\lesssim 5\%$, and the achieved total net exposure was 69.5 ks.

The contribution of cosmic X-ray background (CXB; Boldt 1987) was estimated using the HXD-PIN response for diffuse emission. We adopted the form of CXB determined by HEAO 1 (Gruber et al. 1999); $9.0 \times 10^{-9} \times (E/3 \text{ keV})^{-0.29} \times \exp(-E/40 \text{ keV})$ erg cm^{-2} s^{-1} str^{-1} keV^{-1}, where E is the photon energy. The CXB count rate is estimated to be $\sim 9\%$ of the net source signals. Recent works find that the CXB normalization is higher by ~ 10–15% at ~ 10–100 keV, than that of Gruber et al. (1999) (Revnivtsev et al. 2003, Churazov et al. 2007). This level of uncertainty, however, corresponds to only $\sim 1\%$ of the net source flux of NGC 4945, and does not affect the subsequent results on the high energy spectrum.

We show in figure 2 the energy spectra of NGC 4945 observed with HXD-PIN (below 60 keV), in comparison with HXD-PIN background which includes both NXB and the CXB. As shown in the lower panel of figure 2, the net source counts exceed $\sim 20\%$ of the background over the entire HXD-PIN energy range. In the following spectral analysis, we use an energy range of 12–60 keV, in which the source signals are detected at $> 8\sigma$ above the background in each of appropriately summed energy bins in the spectrum. We use the response matrix of version `2006-8-14`, which is appropriate for the HXD nominal aiming position. The background-subtracted source count rate in the energy range, with statistical error, is 0.299 ± 0.003 cts s^{-1}, which is $\sim 65\%$ of the background rate (NXB plus CXB, 0.461 ± 0.001 cts s^{-1}).

The source and background spectra from HXD-GSO were extracted in the same way as for HXD-PIN. We further applied the instrumental dead-time correction to the background spectrum as well, which was not necessary in the case of HXD-PIN. We present in figure 2 the AGN energy spectrum taken with HXD-GSO (above 50 keV). The HXD-GSO background does not include the CXB, which is negligible in this case. Figure 2 (bottom) show that even in the HXD-GSO range, the signal exceeds 2% of the background up to ~ 150 keV, although it decreases to $\lesssim 1\%$ at ~ 200 keV. Systematic studies on the modeled background spectrum of HXD-GSO shows that its uncertainty is $\sim 2\%$ (Takahashi et al. 2007), so that we can claim the detection of this source up to 150 keV at present. We use the response matrix of version `2006-3-21` and arf file `ae_hxd_gsohxnom_crab_20070502.arf` (Takahashi et al. 2007), which are appropriate for the HXD nominal

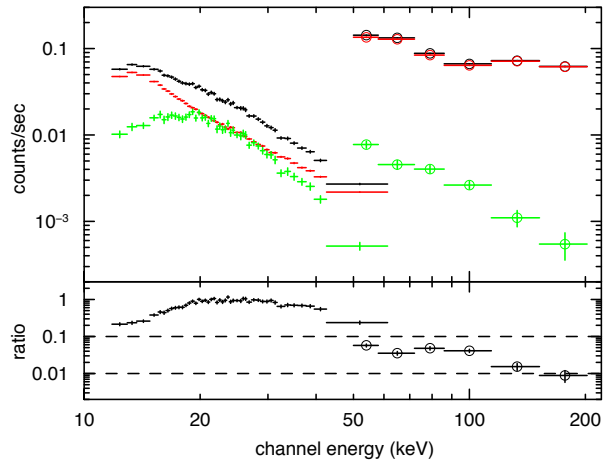

Fig. 2. HXD spectra from the present Suzaku observation of NGC 4945. The PIN and GSO data points are indicated by crosses and circles, respectively. In the upper panel, the total spectra (source plus background) are shown in black, the estimated background spectra in red, and the net source (total minus background) spectra in green. The lower panel shows the ratio of the net source to the background spectra.

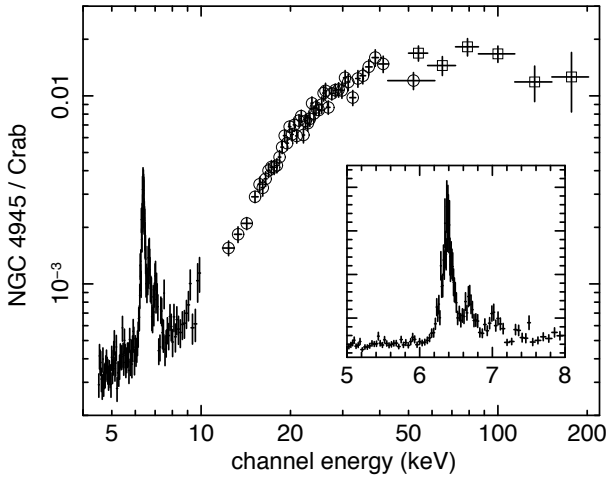

Fig. 3. The background-subtracted Suzaku spectra of the nucleus of NGC 4945, normalized to those of the Crab nebula. The XIS-FI, PIN and GSO data points are marked with crosses, circles and squares, respectively. (Inserted figure) A zoom of the 5–8 keV band, with the flux in linear scale. The XIS-BI data are omitted just for clarity.

aiming position. In the subsequent spectral analysis, we utilize the GSO data only in the 70–120 keV range, because of the current uncertainties in the HXD-GSO background and response, in the > 120 keV and 50–70 keV energies, respectively.

2.3. Broadband Spectrum

Figure 3 shows the source spectra in the 4.5–200 keV band, normalized to those of the Crab nebula taken with Suzaku on 2006 September 15 at the HXD nominal aiming position. The total net exposure onto the Crab was ~ 12 ks with the XIS, and ~ 10 ks with the HXD. Since the energy spectrum of the Crab is known to be a single power-law with a photon index of ~ 2.1, the ratio spectrum can be regarded as an approximate $\nu F\nu$ spectrum. Figure 3 reveals an extremely hard spectrum in the ~ 10–30 keV band, which indicates that the underlying emission is attenuated by a considerable degree of absorbing column. Above ~ 40 keV, the Crab ratio stays rather constant up to ~ 200 keV, without showing clear evidence for any high-energy spectral cutoff.

The continuum below ~ 10 keV is softer but still quite hard ($\Gamma \sim 1$), so that it can be better interpreted as a reflected continuum rather than an intrinsic emission. This inference is supported also by the strong emission line features, which are clearly seen around 6–8 keV in the inserted figure.

3. Broad-Band Spectral Fitting

3.1. Baseline Continuum Model

As described in §1, the nuclear intrinsic emission is considered to appear only above ~ 10 keV, while its reprocessed emission dominates the energy spectrum below 10 keV. As an approximation to the 4.5–50 keV spectrum, we then adopted an baseline continuum (BC) model consisting of an absorbed power-law with high energy exponential cutoff ($\gtrsim 100$ keV), and a reflection continuum by a cold matter which is absorbed by the Galactic column (1.57×10^{21} cm^{-2}; Heiles & Cleary 1979) only. We multiplied the first component by an energy-dependent factor of the form $\exp\{-N_{\rm H}\sigma(E)\}$, where the cross-section $\sigma(E)$ includes the effects of both photo-electric absorption (model `wabs` in XSPEC) and Compton scattering (model `cabs` in XSPEC). The latter component is based on an assumption that some fraction, $f_{\rm refl}$, of the primary power-law is reflected from cold material, and reaches us without further absorbed by the obscuring matter which affects the first component. We modeled the cold reflection using `pexrav` in XSPEC (Magdziarz & Zdziarski 1995), where the continuum shape Γ was tied to that of the intrinsic power-law. The inclination (i) of the reflector was set to 60°, and the iron abundance ($A_{\rm Fe}$) was fixed at 1. The `pexrav` model was used in such a way that it produces the reflected photons only, because the illuminating primary continuum is separately modeled. The model reproduce a neutral iron edge structure at ~ 7.1 keV, while it does not include any fluorescent lines, although their occurrence is physically expected.

The data and the best-fit BC model are shown in the top panel of figure 4. The spectrum up to 10 keV is dominated by the cold reflection component, while the luminous intrinsic power-law appears above that energy. The cutoff energy is constrained to be 200^{+150}_{-50} keV in the fit. However, when the GSO background systematic error ($\sim 2\%$) are taking into account, we get only its lower limit of ~ 80 keV.

The bottom panerl of figure 4 shows the data/model ratio around the iron line region. It reveals several emission lines, at ~ 6.40 keV, ~ 6.70 keV, ~ 7.05 keV, and possibly at ~ 7.47 keV. We therefore added Gaussians to repre-

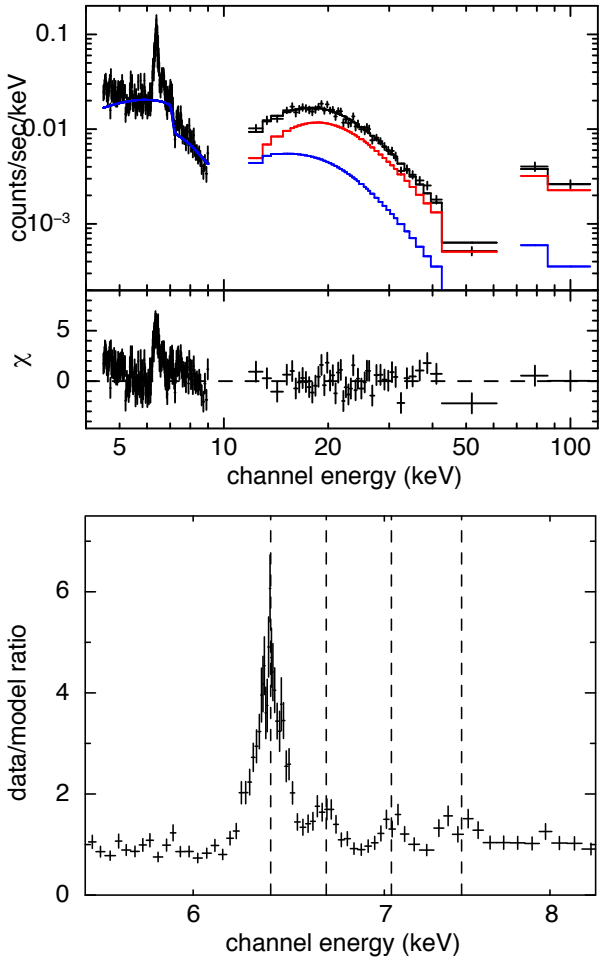

Fig. 4. (Top) The broad band (4.5–120 keV) Suzaku spectrum of NGC 4945. The data and the baseline continuum model (see text) are shown. The models are shown in colored lines; the absorbed intrinsic power-law in red, the reflection component in blue, and their sum in black. (Bottom) The data to model ratios from this fit in the 5.5–8.2 keV band.

sent those four features, and found that all of them are statistically significant ($\gtrsim 3\sigma$ even with the ~ 7.47 keV one). In addition, the fitted center energies of three of them, $6.396^{+0.005}_{-0.005}$, $7.06^{+0.03}_{-0.04}$, and $7.45^{+0.05}_{-0.07}$ keV (here and hereafter in the source rest-frame energies, assuming $z = 0.0019$), agree with those of Fe I Kα, Fe I Kβ and Ni I Kα lines, respectively. This indicate that they originate as fluorescence from cold materials. Note that the latter two emission lines have not been detected by any previous missions. Apart from the three neutral lines, the emission line at $\sim 6.676^{+0.025}_{-0.020}$ keV agrees in energy with Fe XXV Kα line, suggesting the presence of another reprocessing material which is highly-ionized.

We show in figure 5 the $\nu F\nu$ spectrum, on which the fitted model is superposed. The best-fit parameters of the BC plus Gaussian lines are summarized in table 1. The model reproduces the observed continuum marginally successfully (χ^2/d.o.f. $= 330/242 \sim 1.4$), though systematic residuals are recognized (figure 5 bottom) around ~ 5 keV and ~ 9 keV.

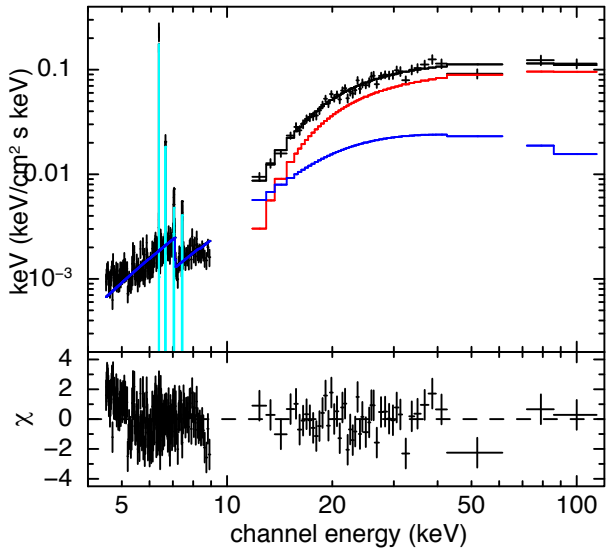

Fig. 5. (Top) The broad band (4.5–120 keV) $\nu F\nu$ spectrum of NGC 4945, on which BC model is superposed. The data are shown in black points and the models in colored lines; the absorbed intrinsic power-law in red, the cold reflection component in blue, and emission lines in cyan. (Bottom) The residuals from this fit.

3.2. BC plus Thermal Plasma Model

The ionized material from which the Fe XXV Kα line originates may alternatively be a hot plasma collisionally heated by the star-burst activity around the nucleus (Schurch et al. 2002). We thus added to the BC model a hot plasma component (`mekal` in XSPEC). We separately modeled the three neutral lines; the Fe I Kβ and Ni I Kα lines by single Gaussians, while we used the following model for the strong Fe I Kα line. The model consists of two Gaussian lines, Kα_1 (6.404 keV) and Kα_2 (6.391 keV), and also includes a Compton down-scattered shoulder, which is physically expected when the line is produced in optically-thick re-processing materials (Matt 2002). The profile of the shoulder was calculated according to Illarionov et al. (1979), while its normalization was allowed to vary. The ratio between the normalization of the shoulder and that of the narrow core is quoted as $f_{\rm CS}$ hereafter. The center energies of the Fe I Kβ and Ni I Kα line were fixed at 7.06 keV and 7.47 keV, and their normalization were also fixed at 12% and 5% of that of Fe I Kα, respectively. The fit goodness was significantly improved (χ^2/d.o.f. $= 257/247$) compared to the BC model, mainly due to the inclusion of the hot plasma. We show in figure 6 the $\nu F\nu$ spectrum on which the fitted model is superposed. The best-fit parameters are summarized in table 1.

The Fe I Kα line has an equivalent width of $1.3^{+0.5}_{-0.2}$ keV with respect to the cold reflection component. This is consistent with the prediction in the case when the line and reflected continuum originate at the same location, possibly a visible part of the putative torus (e.g. Matt et al. 1996). With the column density of $N_{\rm H} \gtrsim$ a few $\times 10^{24}$ cm^{-2}, the

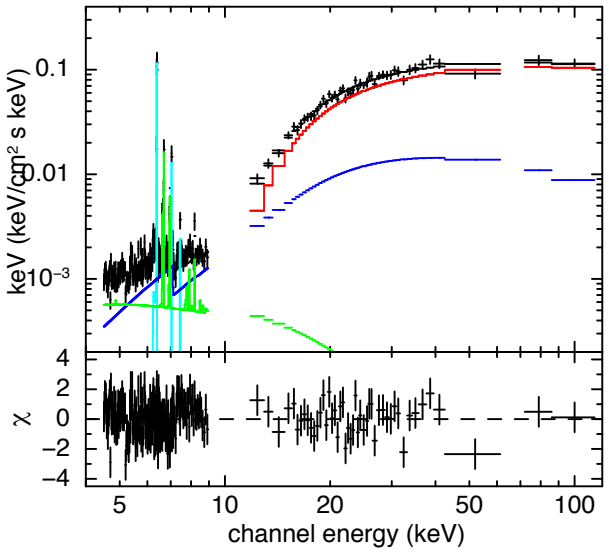

Fig. 6. The same as figure 5, but for the BC + thermal plasma model. The data are shown in black points and the models in colored lines in the top panel; the absorbed intrinsic power-law in red, the cold reflection component in blue, the thermal plasma in green, and emission lines in cyan.

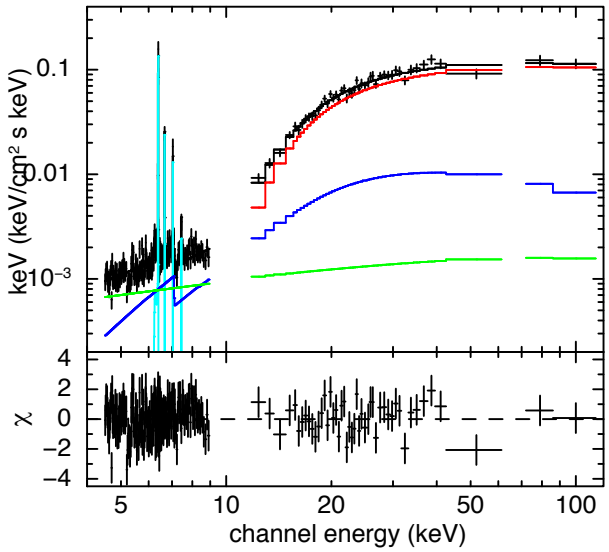

Fig. 7. The same as figure 5, but for the BC + scattered power-law model. The green line shows the continuum scattered by a highly ionized scatterer.

electron scattering suppresses the intrinsic emission by a factor of $\exp\{-N_{\rm H}\cdot\sigma_{\rm T}\}$. Thus $f_{\rm refl}$, calculated as a ratio between the normalization of `pexrav` and that of the absorbed power-law, is in reality much smaller than would be read on figure 6, and becomes $\sim$ a few $\times 10^{-3}$. The Compton shoulder parameter $f_{\rm CS}$ is constrained to be $\sim 0.11^{+0.07}_{-0.10}$, which is consistent with those from re-processing by a near-Compton-thick reflector though slightly smaller than expected value (~ 0.20); see Matt (2002) for calculation, and e.g. Pounds & Vaughan (2006) and Pounds & Page (2005) for observational evidence in NGC 1068 and MKN 3, respectively.

3.3. BC plus Scattered Continuum Model

Recent studies with high resolution instruments show radiative recombination continua, which provide clear evidence for photo-ionized gas. These atomic features are typically seen in the highest signal–to–noise spectra of obscured AGNs (e.g. the compilation of Bianchi et al. 2006, Young et al. 2001; Kinkhabwala et al. 2002). According to detailed calculations of the column, ionisation state and covering fraction of the gas required to produce the radiative recombination continuua and the copious low energy photo-ionised lines in Seyfert 2's, such material must necessarily also scatter some fraction $f_{\rm scatt}$ of the photo-ionizing flux, producing a continuum which has approximately the same shape as the incident AGN emission, i.e. a power law (Bianchi et al. 2006). This continuum can be seen directly in regions of the spectrum away from the strong line emission (e.g. Mkn 3: Bianchi et al. 2005b). Hence we explore here the possibility that the Fe XXV Kα line seen in NGC 4945 is from photo-ionized rather than collisionally ionized material, although the RGS data, hampered by poor signal–to–noise ratio of this object at low energies, did not give strong evidence for such a photo-ionized gas (Guainazzi & Bianchi 2007).

We thus added to the BC model, another power-law absorbed only by the Galactic column, with its photon index set to be the same as the primary one. We modeled the neutral lines in the same way as in §3.2, while the Fe XXV Kα line with a single Gaussian, allowing its energy to vary. This model has also reproduced the data successfully, with a significantly better χ^2 than the previous one (χ^2/d.o.f. $= 241/246$). We show in figure 7 the $\nu F\nu$ spectrum on which the fitted model is superposed. The obtained best-fit parameters are shown in table 1. We show in figure 8 confidence contours of the primary continuum slope, Γ, vs the absorption column density, calculated under this model.

The equivalent width of the Fe I Kα line, with respect to the cold reflection, is calculated at $1.6^{+0.3}_{-0.3}$ keV. Adding another Gaussian at 6.96 keV, corresponding to Fe XXVI Kα, did not improve the fit. The equivalent widths of the Fe XXV Kα and Fe XXVI Kα lines, with respect to the scattered power-law, is ~ 0.5 keV and < 0.1 keV, respectively.

In either of the BC + thermal or the BC + scattered PL modeling, an unphysical trade-off between cold reflection continuum and thermal/scattered PL component may happen. We thus calculated the 5–10 keV flux of the cold reflection continuum, and obtained $7.8^{+1.0}_{-1.2}\times 10^{-13}$ erg s^{-1} cm^{-2}, for each of the BC + thermal or BC + scattered PL model. This value agrees well with that obtained using Chandra ACIS, from the nucleus and a surrounding region of $\sim 5''$ scale ($8.0^{+1.3}_{-1.5}\times 10^{-13}$ erg s^{-1} cm^{-2}, Done et al. 2003).

Table 1. Best-fit parameters of the three models (see text) to the Suzaku XIS, HXD-PIN, and HXD-GSO spectrum of NGC 4945.

Model Component	Parameter	BC + lines	BC + Thermal	BC + Scattering
Intrinsic PL	Γ	$1.6^{+0.1}_{-0.1}$	$1.5^{+0.2}_{-0.1}$	$1.6^{+0.1}_{-0.2}$
	$N_{\rm PL}$*	$3.0^{+1.5}_{-1.5}$	$1.4^{+0.7}_{-0.7}$	$1.7^{+1.0}_{-0.7}$
	$E_{\rm cut}$†	200^{+150}_{-50}‡‡	150^{+100}_{-50}‡‡	190^{+150}_{-50}‡‡
	$N_{\rm H}$‡	$6.0^{+0.5}_{-0.5}$	$5.4^{+0.4}_{-0.4}$	$5.3^{+0.4}_{-0.9}$
Reflection	$f_{\rm refl}$	$3^{+3}_{-2}\times10^{-3}$	$3^{+2}_{-1}\times10^{-3}$	$3^{+1}_{-1}\times10^{-3}$
Mekal	kT§	-	$7.1^{+1.0}_{-0.9}$	-
	norm‖	-	$1.2^{+0.1}_{-0.2}\times10^{-3}$	-
Scattered PL	$f_{\rm scat}$	-	-	$\sim2\times10^{-4}$
Fe I Kα	$E_{\rm c}$#	$6.396^{+0.005}_{-0.005}$	see text	see text
	I**	29^{+2}_{-2}	31^{+2}_{-2}	32^{+2}_{-2}
	EW††	~0.6	$1.3^{+0.5}_{-0.2}$§§	$1.6^{+0.3}_{-0.3}$§§
CS	$f_{\rm CS}$	-	$0.11^{+0.07}_{-0.10}$	$0.10^{+0.08}_{-0.09}$
Fe XXV Kα	$E_{\rm c}$#	$6.675^{+0.025}_{-0.020}$	-	$6.683^{+0.015}_{-0.015}$
	I**	$6.0^{+1.5}_{-1.2}$	-	$8.4^{+1.0}_{-1.5}$
	EW††	~0.2	-	0.5^{+*}_{-*}
Fe I Kβ	$E_{\rm c}$#	$7.06^{+0.03}_{-0.04}$	7.06 fixed	7.06 fixed
	I**	$2.9^{+1.2}_{-1.3}$	-##	-##
	EW††	~0.1	~0.2§§	~0.2§§
Ni I Kα	$E_{\rm c}$#	$7.45^{+0.05}_{-0.07}$	7.47 fixed	7.47 fixed
	I**	$2.7^{+1.0}_{-1.0}$	-***	-***
	EW††	~0.1	~0.1§§	~0.1§§
χ^2/d.o.f.		330/242	257/247	241/246

* photons keV^{-1} cm^{-2} s^{-1} at 1 keV. †keV. ‡10^{24} cm^{-2}. §keV. ‖ #Center energy in keV.
**10^{-6} photons cm^{-2} s^{-1}. ††keV. ‡‡ Only lower limit of $\sim$ 80 keV is obtained when the GSO background systematics are taking into account.
§§ EW with respect to the cold reflection continuum. ‖‖Upper limit.
##Set equal to 12% of that of Fe I Kα. ***Set equal to 5% of that of Fe I Kα.

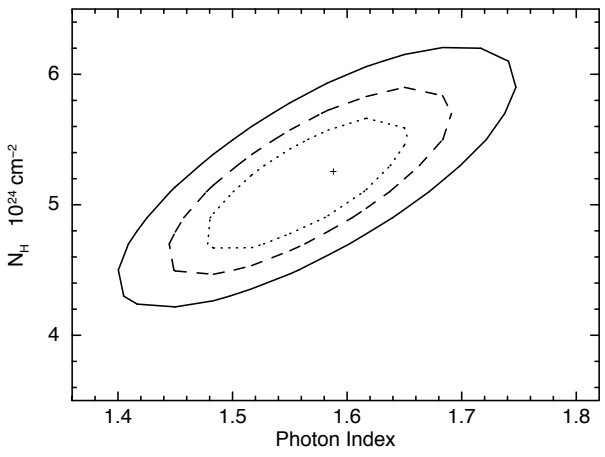

Fig. 8. Confidence (68%, 90%, 99%) contours of the photon index Γ of the primary continuum vs. the absorption column $N_{\rm H}$, calculated under the "BC + Scattered Continuum" model.

4. Broadband Time Variability

Figure 9 shows light curves of NGC 4945 taken with Suzaku in five energy ranges. In the upper two panels (with the XIS), the data are binned at the orbital period (5760 sec), while in the other three panels (with the HXD) each time bin corresponds to a continuous time interval which is free from any data gap. The bin length in the latter case is typically 700–1500 sec, since HXD "cleaned events" suffer from two data gaps per spacecraft orbit ($\sim$ 5760 sec), mainly due to passages through high background regions (at high magnetic longitudes and near the SAA). We discarded data points shorter than 512 sec, since they have too large statistical errors. The two light curves below 10 keV are consistent with being constant. In the energy ranges above 10 keV, in contrast, we observed that the source varied by a factor of $\sim$ 2 within $\sim$ 20 ks. This agrees with the picture that the reflection from a distant cold material (plus possibly an extended thermal emission or scattering from an ionized medium) dominates the spectrum below 10 keV, while we are seeing

the intrinsic AGN emission in the higher energy.

In order to search the spectra for intensity-correlated changes, we divided the entire observation period into two phases according to the 25–50 keV count rate; "high flux" and "low flux" phases, corresponding to periods when the count rate is higher and lower than 0.75 cts s^{-1}, respectively. The net exposure is 33.7 ks for the high flux phase and 31.7 ks for the low phase. Figure 10 shows the spectra of the two phases, in the form of their ratios to the time-averaged spectrum. Above 10 keV, the flux of the high phase is approximately twice as high as that of the low phase, independent of energy. In contrast, data points below 10 keV show no significant difference between the two phases, in agreement with the implication of the light curves.

We fitted each spectrum of the two phases by the BC + scattered power-law model, and confirmed that the spectral parameters do not significantly change as the flux varied, except for the normalization of the absorbed power-law component.

It is quite interesting to obtain the varying spectral component, since it must be the pure intrinsic AGN emission without being diluted by any re-processed component. Actually with the HXD, we were able to carry out this analysis in the present case. We show in figure 11 the differential spectrum between the two phases, i.e. a spectrum of the high flux phase minus that of the low phase. As shown there, an absorbed power-law reproduces the data successfully (χ^2/d.o.f. $= 141/216$), with $\Gamma = 1.6^{+0.2}_{-0.3}$, $N_{\rm H} = 4.5^{+0.5}_{-1.0} \times 10^{24}$ cm^{-2}, and $E_{\rm cut} \gtrsim 150$ keV (not constrained). These parameter values agree with those we have derived from the time-averaged spectrum in the previous section. This confirms that the intrinsic component is quite dominant in the time-averaged spectrum, in the energy above ~ 10 keV, and that the direct nuclear emission maintains its spectral shape as it varies.

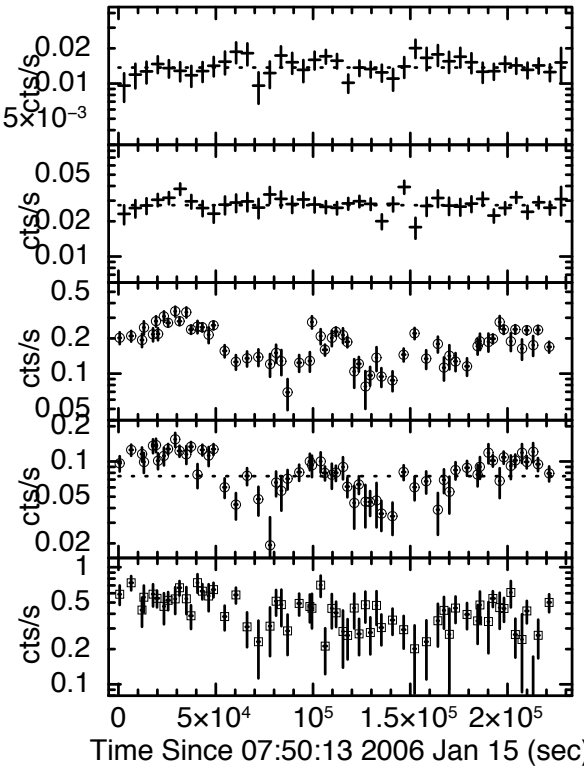

Fig. 9. Background-subtracted light curves of NGC 4945 taken with Suzaku. The top and second panels show those in 6.25–6.52 keV and 6.5–9.0 keV, respectively, taken with the four XIS sensors, and re-binned with the orbital period of 5760 s. The third, fourth, and bottom panels shows 12–25 keV, 25–50 keV (HXD-PIN), and 52–114 keV (HXD-GSO) light curves, respectively. In these panels, each bin corresponds to a continuous time interval without data gaps. Dotted line in the top, second and the fourth panels correspond to 0.015 cts s^{-1}, 0.027 and 0.075 cts s^{-1}, respectively.

5. Discussion

5.1. The Hard X-ray Emission

In the hard X-ray ($\sim$ 4.5–120 keV) band, the AGN emission from NGC 4945 clearly exhibits at least two distinct spectral components. One can be identified as the AGN primary emission transmitting through the Compton-thick absorber. This component was observed above ~ 10 keV, showing rapid time variability during the observation. The spectrum is well reproduced by heavily absorbed power-law. The other is dominant below ~ 10 keV, without showing any time variability. The spectrum is characterized by a hard continuum along with an edge structure and neutral/ionized fluorescence lines from heavy metals, suggesting its production in re-processing materials around the AGN.

The best-fit parameters of the primary power-law, $\Gamma = 1.6^{+0.1}_{-0.2}$ and $N_{\rm H} = 5.3^{+0.4}_{-0.9} \times 10^{24}$ cm^{-2}, agree with those derived by the previous hard X-ray missions (Iwasawa et al. 1993, Madejski et al. 2000, Guainazzi et al. 2000). The absence of variability in the absorbing columns over several years suggests the location of the absorber, namely,

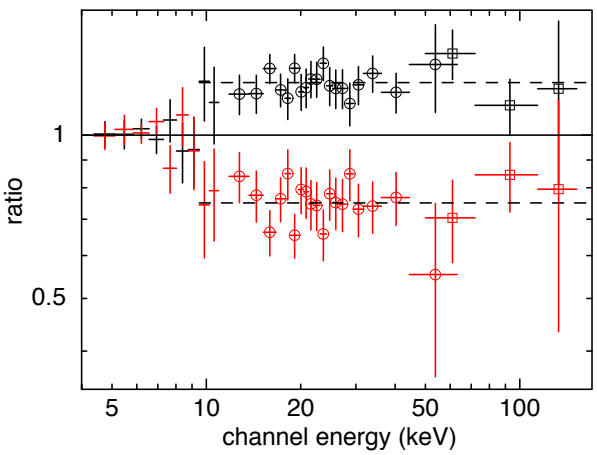

Fig. 10. Spectra from the "high phase" (black) and "low phase" (red), shown as their ratios to the time averaged spectrum. The XIS, HXD-PIN and HXD-GSO data points are shown in crosses, circles, and squares, respectively.

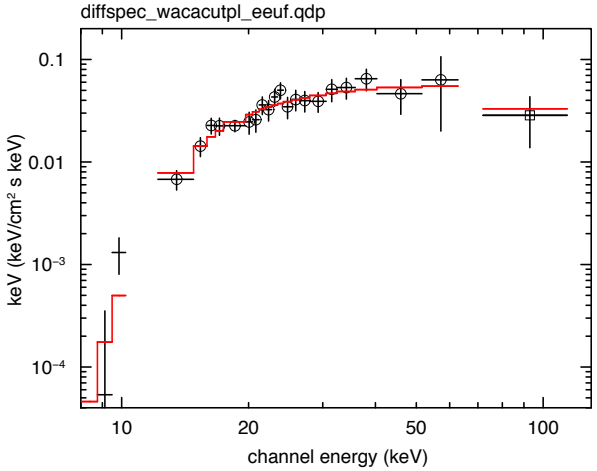

Fig. 11. Differential $\nu F\nu$ spectrum between the two phases (black points), i.e. high minus low. on which an absorbed power-law model with $\Gamma = 1.6$ is superposed (red line).

at a distance in excess of a light year from the nuclear continuum source. The spectral index of ~ 1.6 lie at the relatively flat end of the distribution among Seyfert galaxies (e.g. Turner et al. 1997). We cannot constrain the high energy spectral cutoff. Although it is required in the broad band fitting around 200 keV (see table 1), when the systematic error on the GSO background modeling (2%) is taken into account, we obtain only its lower limit of ~ 80 keV. Nonetheless, a cutoff energy around 100-300 keV is consistent with the one Guainazzi et al. (2000) obtained from this source, and those measured in several Seyfert 1s (e.g. Madejski et al. 1995, Zdziarski et al. 1995, Guainazzi et al. 1999a, Guainazzi et al. 1999b, Perola et al. 1999).

5.2. The Absorbing Material

The observed average 10–50 keV flux was 1.6×10^{-10} erg s^{-1} cm^{-2}, which is ~ 1.6 and ~ 0.9 times that measured by RXTE and BeppoSAX, respectively. At the level of $N_{\rm H} \sim 4 - 5 \times 10^{24}$ cm^{-2}, the optical depth to electron scattering will become rather high, ~ 3 or so. In such a case, the observed spectrum and flux would depend significantly on the geometry of the absorbing matter (Leahy et al. 1989), even though the intrinsic luminosity is the same. The model `cabs` assumes a configuration where a small blob of matter scatters some of the primary flux out of the line of sight. If, on the contrary, the re-processing matter has a large solid angle to the central source, a fraction of the photons will also be scattered into the line of sight, and the nuclear luminosity required to explain the observed flux will decrease. At the same time, such scattered photons would significantly dilute the time variability of the intrinsic source. Based on the observed rapid (less than 1-day) hard X-ray variability in NGC 4945, Madejski et al. (2000) argued that the Compton-thick absorber must be geometrically-thin, with a half angle of less than 10° as seen from the central source. If this is the case, the configuration assumed by `cabs` is considered to be more realistic.

While the present data strongly points to a geometrically thin absorber, the scenario requires a relatively high nuclear intrinsic luminosity. The extrapolation of the best-fit model to the 2–10 keV band, corrected for photo-electric absorption alone, yields a flux of $\sim 1.3 \times 10^{-10}$ erg s^{-1} cm^{-2}. Further correcting this for the Thomson opacity, i.e. multiplying a factor $\exp(\tau_{\rm es})$ where $\tau_{\rm es} = 1.21 N_{\rm H} \sigma_{\rm Th}$, we obtain $\sim 8 \times 10^{-9}$ erg s^{-1} cm^{-2}, and hence a 2–10 keV intrinsic luminosity of $\sim 1 \times 10^{43}$ erg s^{-1}. Using the bolometric corrections of Marconi et al. (2004), a bolometric luminosity of $\sim 2 \times 10^{44}$ erg s^{-1} is derived, which in turn is $\sim 100\%$ of the Eddington limit. Although the inferred $L/L_{\rm Edd}$ is unplausibly large, this value is strongly dependent on $N_{\rm H}$, and there is also some scatter in the bolometric corrections (Marconi et al. 2004). Thus we can also get $L/L_{\rm Edd} \sim 30\%$ within errors, and hence the scenario is energetically feasible. The derived bolometric luminosity is of the same order of magnitude as the observed infrared luminosity of the nucleus (Sanders et al. 2003), and hence the AGN can dominate the energy output from the nucleus.

The flux of the intrinsic emission in the 12–50 keV band showed variations by a factor of 2 on a time scale of $\sim$ 20 ks. Similar variability was observed with every previous mission (Ginga, BeppoSAX, RXTE). From the 12–50 keV light curve, we calculated excess variance $\sigma^2_{\rm NXS}$ (Nandra et al. 1997) in the same manner as O'Neill et al. (2005), to find $\log(\sigma^2_{\rm NXS}) \sim -1.3 \pm 0.1$. This value lies well on the $M_{\rm BH}$ vs $\sigma^2_{\rm NXS}$ relationship derived from a number of Seyfert 1 AGNs; the expected $\log(\sigma^2_{\rm NXS})$ for $M_{\rm BH} = 1.4 \times 10^6 M_\odot$ is -1.25 (O'Neill et al. 2005). This implies that the intrinsic variability is not diluted by scattered photons, and supports the idea that the re-processing material be geometrically-thin.

5.3. The Reflecting Materials

The spectrum below 10 keV showed evidence of reflection from cold matter, and was modeled with a hard reflection continuum and neutral emission lines. The derived equivalent width of the Fe I Kα line, ranging $\sim 1.3 - 1.6$ keV, is consistent with those expected when the line is produced in an optically-thick material with solar abundance (ranging between 1.3 keV and 2.7 keV, Matt et al. 1996). This suggests that the Fe Kα I line and the reflection continuum are generated by the same material (see also Schurch et al. 2002; Done et al. 2003). We note that Guainazzi et al. (2000) preferred a transmission origin for the line as the spectrum below 7 keV is not well fit by reflection alone. However, this is due to there being additional complex low energy emission from hot gas (some of which can be spatially resolved e.g. Done et al. 2003). Our detection of the compton shoulder at $f_{CS} \sim 0.10$ confirms a reflection origin, as transmission predicts $f_{CS} \sim 0.3$ (Matt 2002). The upper limit of $f_{CS} < 0.17$ also indicates that the reflector is probably seen nearly edge on (Matt 2002). We also detect for the first time the associated Fe I Kβ and Ni I Kα lines from the reflector. The flux of

these lines are 10^{+3}_{-3} % and 10^{+5}_{-5} % of that of Fe I Kα, respectively, which also agree with the value expected from the neutral reflection.

The obtained R is quite small at a few $\times 10^{-3}$. As mentioned in §5.1, the estimation of the intrinsic flux, and hence of R, is strongly affected by the geometry of the Compton-thick absorber. In the most extreme case, i.e. when the absorber is spherically surrounding the continuum source, the intrinsic flux would be 3–6 times lower than derived here (Matt et al. 1999, Madejski et al. 2000). Even in that case, R still remains $\lesssim$ a few $\times 10^{-2}$, which is significantly smaller than those of the other Compton-thick Seyfert 2 AGNs; e.g. $R = 1.2-1.4$ in MKN 3 (Pounds & Page 2005, Awaki et al. 2007). This might be explained by assuming the reflector to be located nearly edge-on angle; so we fitted the spectrum with $i = 85°$, to find that the R value increases by only a factor of ~ 2. The small R implies that we see in the reflection only a small part of the illuminated disk on the far side of itself.

All the above evidence on the re-processed signals implies that the geometrically-thin/disk-like reflector is viewed from a near edge-on angle. Considering that the H_2O megamaser emission requires an edge-on inner disk geometry in this source (Greenhill et al. 1997), the simplest explanation of the reflector, absorber and maser source is that these are all the same structure, namely the accretion disk (Madejski et al. 2000, Madejski et al. 2006). Thus the accretion structure in this source could be different from a typical AGN which is considered to have a putative torus with a large covering factor.

5.4. The Ionized Iron Line –Consistency Check–

Another remaining question is the origin of the ionized Fe line observed at $6.683^{+0.015}_{-0.015}$ keV. The BC + Scattered power-law model gives a slightly better fit than the BC + thermal model, to the spectral curvature around 4 keV. However, this is probably simply due to there being more free parameters in this model, and it is thus difficult to provide any clearcut preference on the origin of the soft X-ray continuum and the ionized line from our data. In this section, we therefore only discuss physical consistency of each of our scenarios.

From its energy, the ionized line is consistent with the resonance line, w, at 6.700 keV or the intercombination lines, $x + y$, at 6.682 and 6.668 keV, or their mixture. A strong contribution from the forbidden line, z, at 6.637 keV, is clearly ruled out by the mean line energy. Collisionally ionized plasmas have $G \equiv (x + y + z)/w \sim 1$ while a pure photo-ionized plasma has $G > 1$ as the resonance line is weak. Note that contamination from dielectronic lines is not important at the inferred temperature of ~ 7 keV (Oelgoetz & Pradhan 2001). However, continuum photons enhance w through resonance line scattering, so the observed line energy can also be consistent with photo-ionization (Bianchi et al. 2005a).

The temperature of $6-8$ keV estimated from the thermal plasma model is rather high compared to those expected from ordinary star-burst activity ($\sim$ 500 eV), and difficult to produce (Suchkov et al. 1994, Strickland & Stevens 2000). However, a similar temperature was observed in a nearby pure star-burst galaxy NGC 253 (Pietsch et al. 2001). From the scattered continuum model, we obtained $f_{\rm scat} \sim$ several $\times 10^{-4}$. The column density of the photo-ionized gas can be estimated on the basis of this ratio. In order to have an order of magnitude estimate we assume a covering factor of ~ 0.1, then the gas column density would be $10^{21} - 10^{22}$ cm^{-2}. This value lies within those estimated in other obscured AGNs (e.g. Bianchi et al. 2006). The equivalent width of the Fe XXV Kα and Fe XXVI Kα lines with respect to the scattered power-law, i.e. ~ 0.5 keV and < 0.1 keV, respectively, are consistent with the both components originating from a photo-ionized gas (see calculations in Bianchi & Matt 2002; Bianchi et al. 2005a). To highly ionize the iron, the region where the line originates needs to be close to the central source so that its flux could potentially vary as the primary continuum does. We searched in vain for any time variability of the ionized lines.

Therefore, both of our scenarios are considered to be physically consistent. Yet another possibility is that the ionized line, together with the modeled scattered continuum, arise from unresolved point sources (Done et al. 2003).

Acknowledgments

The authors would like to express their thanks to the Suzaku team members. We also thank Dr. Andrzej Zdziarski for his helpful discussions. TI and PG, being research fellows of the Japan Society for the Promotion of Science, thank the Society. GM acknowledges the support by the US Department of Energy contract to SLAC no. DE-AC3-76SF00515, and NASA Suzaku grant no. NNX07AB05G.

References

Antonucci, R. R. J. & Miller, J. S. 1985, ApJ, 297, 621
Awaki, H. & Koyama, K. 1993, Advances in Space Research, 13, 221
Awaki, H., Koyama, K., Kunieda, H., & Tawara, Y. 1990, Nature, 346, 544
Bianchi, S., Guainazzi, M., & Chiaberge, M. 2006, A&A, 448, 499
Bianchi, S. & Matt, G. 2002, A&A, 387, 76
Bianchi, S., Matt, G., Nicastro, F., Porquet, D., & Dubau, J. 2005a, MNRAS, 357, 599
Bianchi, S., Miniutti, G., Fabian, A. C., & Iwasawa, K. 2005b, MNRAS, 360, 380
Boldt, E. 1987, Phys. Rep., 146, 215
Chen, Y. & Huang, J.-H. 1997, ApJL, 479, L23+
Churazov, E. et al. 2007, A&A, 467, 529
Comastri, A., Setti, G., Zamorani, G., & Hasinger, G. 1995, A&A, 296, 1
Done, C., Madejski, G. M., & Smith, D. A. 1996, ApJL, 463, L63+
Done, C., Madejski, G. M., Życki, P. T., & Greenhill, L. J. 2003, ApJ, 588, 763
Gandhi, P. & Fabian, A. C. 2003, MNRAS, 339, 1095
Gilli, R., Comastri, A., & Hasinger, G. 2007, A&A, 463, 79

Greenhill, L. J., Moran, J. M., & Herrnstein, J. R. 1997, ApJL, 481, L23+
Gruber, D. E., Matteson, J. L., Peterson, L. E., & Jung, G. V. 1999, ApJ, 520, 124
Guainazzi, M. & Bianchi, S. 2007, MNRAS, 374, 1290
Guainazzi, M., Matt, G., Brandt, W. N., Antonelli, L. A., Barr, P., & Bassani, L. 2000, A&A, 356, 463
Guainazzi, M., Matt, G., Molendi, S., Orr, A., Fiore, F., Grandi, P., Matteuzzi, A., Mineo, T., Perola, G. C., Parmar, A. N., & Piro, L. 1999a, A&A, 341, L27
Guainazzi, M., Perola, G. C., Matt, G., Nicastro, F., Bassani, L., Fiore, F., dal Fiume, D., & Piro, L. 1999b, A&A, 346, 407
Heiles, C. & Cleary, M. N. 1979, Australian Journal of Physics Astrophysical Supplement, 47, 1
Ikebe, Y., Leighly, K., Tanaka, Y., Nakagawa, T., Terashima, Y., & Komossa, S. 2000, MNRAS, 316, 433
Illarionov, A., Kallman, T., McCray, R., & Ross, R. 1979, ApJ, 228, 279
Ishisaki, Y. et. al. 2007, PASJ, 59, 113
Isobe, N., Kubota, A., Makishima, K., Gandhi, P., Griffths, R., Dewangan, G. C., Itoh, T., & Mizuno, T. 2007, PASJ, 59, 35
Iwasawa, K., Koyama, K., Awaki, H., Kunieda, H., Makishima, K., Tsuru, T., Ohashi, T., & Nakai, N. 1993, ApJ, 409, 155
Iwasawa, K., Yaqoob, T., Awaki, H., & Ogasaka, Y. 1994, PASJ, 46, L167
Kinkhabwala, A., Sako, M., Behar, E., Kahn, S. M., Paerels, F., Brinkman, A. C., Kaastra, J. S., Gu, M. F., & Liedahl, D. A. 2002, ApJ, 575, 732
Kokubun, M. et al. 2007, PASJ, 59, 53
Koyama, K., Inoue, H., Tanaka, Y., Awaki, H., Takano, S., Ohashi, T., & Matsuoka, M. 1989, PASJ, 41, 731
Koyama, K. et al. 2007, PASJ, 59, 23
Leahy, D. A., Matsuoka, M., Kawai, N., & Makino, F. 1989, MNRAS, 236, 603
Madau, P., Ghisellini, G., & Fabian, A. C. 1994, MNRAS, 270, L17+
Madejski, G., Done, C., Życki, P. T., & Greenhill, L. 2006, ApJ, 636, 75
Madejski, G., Życki, P., Done, C., Valinia, A., Blanco, P., Rothschild, R., & Turek, B. 2000, ApJL, 535, L87
Madejski, G. M. et al. 1995, ApJ, 438, 672
Magdziarz, P. & Zdziarski, A. A. 1995, MNRAS, 273, 837
Malizia, A., Bassani, L., Stephen, J. B., Di Cocco, G., Fiore, F., & Dean, A. J. 2003, ApJL, 589, L17
Marconi, A., Risaliti, G., Gilli, R., Hunt, L. K., Maiolino, R., & Salvati, M. 2004, MNRAS, 351, 169
Matt, G. 2002, MNRAS, 337, 147
Matt, G., Brandt, W. N., & Fabian, A. C. 1996, MNRAS, 280, 823
Matt, G., Fabian, A. C., Guainazzi, M., Iwasawa, K., Bassani, L., & Malaguti, G. 2000, MNRAS, 318, 173
Matt, G. et al. 1997, A&A, 325, L13
Matt, G., Pompilio, F., & La Franca, F. 1999, New Astronomy, 4, 191
Mauersberger, R., Henkel, C., Whiteoak, J. B., Chin, Y.-N., & Tieftrunk, A. R. 1996, A&A, 309, 705
Mitsuda, K. et al. 2007, PASJ, 59, 1
Moorwood, A. F. M., van der Werf, P. P., Kotilainen, J. K., Marconi, A., & Oliva, E. 1996, A&A, 308, L1+
Nandra, K., George, I. M., Mushotzky, R. F., Turner, T. J., & Yaqoob, T. 1997, ApJ, 476, 70
Oelgoetz, J. & Pradhan, A. K. 2001, MNRAS, 327, L42
O'Neill, P. M., Nandra, K., Papadakis, I. E., & Turner, T. J. 2005, MNRAS, 358, 1405
Ott, M., Whiteoak, J. B., Henkel, C., & Wielebinski, R. 2001, A&A, 372, 463
Perola, G. C., Matt, G., Cappi, M., Dal Fiume, D., Fiore, F., Guainazzi, M., Mineo, T., Molendi, S., Nicastro, F., Piro, L., & Stirpe, G. 1999, A&A, 351, 937
Pietsch, W. et al. 2001, A&A, 365, L174
Pounds, K. & Vaughan, S. 2006, MNRAS, 368, 707
Pounds, K. A. & Page, K. L. 2005, MNRAS, 360, 1123
Sanders, D. B., Mazzarella, J. M., Kim, D. -C & Surace, J. A. 2003, ApJ, 126, 1607
Revnivtsev, M., Gilfanov, M., Sunyaev, R., Jahoda, K., & Markwardt, C. 2003, A&A, 411, 329
Schurch, N. J., Roberts, T. P., & Warwick, R. S. 2002, MNRAS, 335, 241
Strickland, D. K. & Stevens, I. R. 2000, MNRAS, 314, 511
Suchkov, A. A., Balsara, D. S., Heckman, T. M., & Leitherner, C. 1994, ApJ, 430, 511
Takahashi, H. et al. PASJ, submitted.
Takahashi, T. et al. 2007, PASJ, 59, 35
Turner, T. J., George, I. M., Nandra, K., & Mushotzky, R. F. 1997, ApJ, 488, 164
Ueno, S., Koyama, K., Nishida, M., Yamauchi, S., & Ward, M. J. 1994a, ApJL, 431, L1
Ueno, S., Mushotzky, R. F., Koyama, K., Iwasawa, K., Awaki, H., & Hayashi, I. 1994b, PASJ, 46, L71
Young, A. J., Wilson, A. S., & Shopbell, P. L. 2001, ApJ, 556, 6
Zdziarski, A. A., Johnson, W. N., Done, C., Smith, D., & McNaron-Brown, K. 1995, ApJL, 438, L63